International Journal of Heat and Technology
Vol. 44, No. 1, February, 2026, pp. 307-318
Journal homepage: http://iieta.org/journals/ijht

Experimental and Numerical Investigation of Water Collection and Droplet Dynamics on Bioinspired Surfaces Under Ambient Conditions

Uvarani Aka, Aruna Kumar Behura*

School of Mechanical Engineering, Vellore Institute of Technology, Vellore 632014, India

Corresponding Author Email: arun.behura@vit.ac.in

https://doi.org/10.18280/ijht.440127

Received: 8 November 2025
Revised: 11 February 2026
Accepted: 23 February 2026
Available online: 28 February 2026

Keywords:
condensation, water harvesting, Peltier module, droplet behaviour, relative humidity, surface wettability

ABSTRACT

In this era, the biggest challenge encountered by people is water scarcity, particularly in arid and semi-arid regions. The finest alternative source of fresh water is atmospheric water harvesting through condensation, which offers a promising and sustainable solution. Despite previous studies having investigated droplet condensation behaviour on flat, inclined, and tubular surfaces with varying surface wettabilities, a systematic understanding of the combined influence of surface geometry, wettability (θ), relative humidity (RH), and dry bulb temperature (DBT) on water harvesting rate (WHR) remains lacking. To address this gap, the present study presents a novel investigation of WHR and droplet mobility on the bioinspired curved surface (CS) with respect to wettability, RH, and DBT. The mobility of the condensed droplets has been tracked with two-dimensional numerical simulations using the Volume of Fluid (VOF) method. The results of the present research indicate that CS are much better at collecting water, due to better droplet shedding and surface wettability. Numerical results are aligned with the experimental data, indicating that surface geometry and environmental conditions affect the condensation. WHR increased with the increase of RH and DBTs due to enhanced vapor pressure differential. Superhydrophilic surfaces achieved the highest WHR among hydrophilic, hydrophobic, and superhydrophobic surfaces. These findings highlight the potential of bioinspired curved surfaces for efficient WHR from the atmosphere.

1. INTRODUCTION

The primary source of every living being on the earth is water. The availability of freshwater resources has become the most significant challenge worldwide and will worsen in the coming years [1, 2]. The continuous growth of population, climatic variations, urbanisation, and industrialisation put pressure on the availability of freshwater resources [3]. Therefore, many researchers have investigated this problem of getting enough water with various methods all over the world. These methods include seawater desalination, wastewater treatment, sewage recycling, and atmospheric water harvesting. However, the desalination method, wastewater treatment method, and recycling of sewage methods are not usable these days due to high installation costs, environmental problems, and transportation issues [4]. Thus, the atmospheric water harvesting method is considered a new solution for producing fresh water at an affordable cost and with minimal energy consumption.

The atmospheric water harvesting method is the process of obtaining fresh water by capturing water droplets from moisture in the atmospheric air. This method is the safest way to generate water because it has no negative influence on the environment and is economically viable. Water droplets absorbed from atmospheric moisture can be replenished by the water cycle on Earth. Thus, the atmospheric water harvesting method is a new and reliable solution to transport fresh water to remote, affected, arid, and semi-arid regions. Many organisms in arid and semi-arid regions, including beetles, cacti, spiders, trees, etc., collect water droplets from moisture through their body surface structures. The beetle's surface structure consists of hydrophilic bumps and hydrophobic valleys. The hydrophilic bumps on the beetle's back capture water droplets in the atmospheric air, and hydrophobic valleys aid in removing the water droplets from the surface. This peculiarity on the surface of the beetle aids in absorbing water droplets in any season. This natural process occurs independently without any aid of an external source through their bumps and valleys [5]. The collected water droplets on the beetle's surface are transported to its mouth when the beetle comes to a fog-basking position [6]. Similarly, the spider web also collects water droplets when it is exposed to moist air in the early mornings. Specifically, the fibre from the spider *Uloborus walckenaerius* forms the periodic spindle knot and joints when the spider web is exposed to misty air. Owing to the unique structural features on the web, condensation of water droplets occurs on the spindle knot due to the generation of surface energy gradient and the variation of Laplace pressure between the spindle knot and joints [7]. A cactus variety of Opuntia microdasys is another organism with a unique capability of collecting water droplets from humid air. When a cactus is exposed to fog, water droplets form on the

tip of the spine and are transported to their trichomes (bottom of spine) through the grooves present in the middle of the spine. The condensation of water droplets from moist air occurs due to the variation of laplace pressure gradient and the surface energy gradient between the tip and the bottom of the spine [8]. These organisms have a distinctive ability to capture water droplets from the atmosphere since their bodies were naturally designed with various features.

Hence, the wettability of these organisms' surfaces plays a vital role in absorbing water droplets from misty air via condensation. The surface wettabilities are classified into four types: superhydrophilic, hydrophilic, hydrophobic, and superhydrophobic states. which are determined by the contact angle between the water droplet and the surface. The surface wettability, contact angle distribution, and the size and shape of the water droplets are all meticulously illustrated in Section 4.1. The high adhesive forces on the superhydrophilic and hydrophilic surfaces follow filmwise condensation, which causes condensed droplets to slide on the surfaces. Similarly, droplets on hydrophobic and superhydrophobic surfaces follow condensation dropwise. Which exhibit rolling or jumping behaviour due to their low adhesive forces [9, 10].

The water droplets on the different structure surfaces with various wettabilities are very promising regarding moisture harvesting. The droplet slides on the wettable surfaces (superhydrophilic and hydrophilic), and the droplets bounce or roll on the non-wettable surfaces (hydrophobic and superhydrophobic). The water droplet mobility on the surface depends not only on the surface wettability but also on surface geometry [11]. Previous studies have demonstrated the importance of surface wettability and the shape of the surface in moisture harvesting. Peng et al. [12] conducted an experiment on the hydrophobic-hydrophilic vertical patterned surface to determine the nucleation rate and droplet diameter on the hybrid surface. The nucleation rate of condensed droplets in the hydrophilic region is higher than in the hydrophobic region. The larger diameter droplets are observed in the hydrophobic region than in the hydrophilic region. The study concludes that the nucleation rate and droplet diameter are indirectly and directly proportional to the contact angle of the surface, respectively. Previous studies have shown that structural modifications of surfaces can influence the droplet behavior and performance [13, 14]. The condensed water droplets with larger diameters in hydrophobic and superhydrophobic regions lead to bounce or rolls on the surfaces [15-18]. Khojasteh et al. [10] observe that the condensed water droplets bounce and roll over the flat inclined superhydrophobic surface with a tilt angle of 30°. Similarly, a numerical study has been conducted on the water droplet movements in a linear flow channel that has been affected by the flowing air properties [19]. Oestreich et al. [20] performed an experiment on the branched surface with heterogeneous wettability by keeping the relative humidity at 80%. The results of this study show that the moisture condensation rate is directly affected by the relative humidity. The condensation rate of moist air depends on relative humidity and other parameters like the dry bulb temperature of moist air [21].

Seo et al. [22] discussed the moisture harvesting performance on the tubular surface subjected to different surface wettabilities. The results show that introducing non-wettable surfaces improves the fog harvesting performance by increasing the water removal rate. The effect of variation of DBT and RH of the moisture air on the surface still needs to be reported. According to currently available literature, it is a challenging task to determine the influence of these characteristics on the moisture harvesting rate. In this study, the VOF method is used to understand the behaviour of the condensed water droplets on a hemispherical curved surface (CS) with a specific range of surface wettabilities and different air properties. The objective of this study is: (1) to understand the behaviour of the condensed water droplets on the hemispherical CS with the variation of relative humidity, dry bulb temperature, and surface wettability; (2) to analyse the condensation rate of a CS at a constant contact angle with variable relative humidity and vice versa.

2. EXPERIMENTAL SETUP AND PROCEDURE

2.1 Experimental setup

The collection of water droplets from the humid air with the help of a Peltier module is based on the concept of condensation phenomena on the cold CS. The schematic diagram of the experimental setup is represented in Figure 1, and the actual experimental setup with all the components involved is shown in Figure 2(a). The condensed water droplets on the CS from the humid air are shown in Figure 2(b).

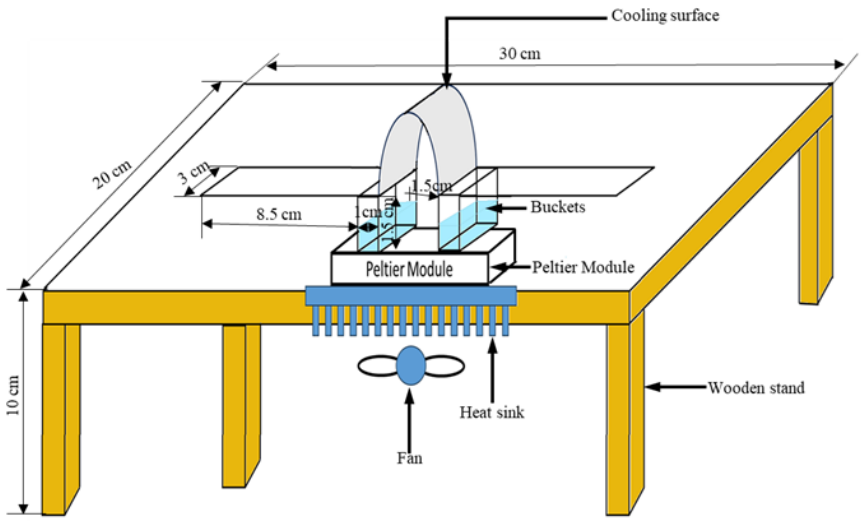

Figure 1. Schematic representation of the experimental setup

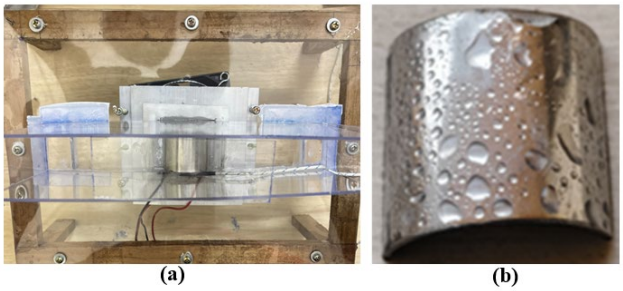

(a) (b)

Figure 2. (a) Top view of the experimental setup, (b) Top view of the cooling surface

In the present work, the experimental setup consisted of a Peltier module, a heat sink, a fan, CS on the cold side, an aluminum thermal bridge, a rectangular polycarbonate sheet, and a wooden stand to hold all these components. The components that help the condensation (Peltier module, CS, thermal bridge) were enclosed in a polycarbonate PVC rectangular cross-section, as shown in Figure 2(a), safely placed on the wooden stand. The heat sink and fan were arranged at the bottom of the polycarbonate sheet. The specifications of the components are detailed in Table 1.

Table 1. Component specifications of the experimental system

Component	Specification
Peltier Module	Max. Current: 5 (A) Max. Voltage: 15 (V)
Cold side	Shape: Curved (semi-circle) Material: Stainless steel Dimension: 15 mm radius
Heat sink	Material: Aluminum Dimension: 12 cm × 10 cm × 2.5 cm

A rectangular polycarbonate sheet is fixed with nuts on the top of the wooden table. The upper part of the rectangular sheet holds the Peltier module, thermal bridge, and cooled CS. A rectangular chamber made with polycarbonate material is placed on the rectangular sheet to protect these components. Whereas, the heat sink and fan are assembled to the hot side of the Peltier module. These parts were placed at the lower part of the rectangular sheet. The hot air passes to the surroundings through the heat sink and fan.

2.2 Experimental procedure

In the present study, a fog harvesting experiment has been performed using a single Peltier module positioned in a controlled airflow generated by a humidifier. The humid air produced by the humidifier streams at 70% relative humidity and 30 ℃ DBT, while the air velocity is maintained at 0.7 m/s across the Peltier cold surface. The Peltier module was mounted on a heat sink assembly, with the CS exposed to the airflow. The humid air conditions were measured using a thermohygrometer. During the test, the electric power supplied to the Peltier module was monitored continuously. Once the airflow and humidity conditions stabilised, the Peltier module started working, leading to the formation of condensate on the cooled surface, which subsequently drained into a collection bucket.

An analytical balance was used to measure the condensate that was collected over an hour for each run. Additionally, the temperature, humidity, airflow velocity, and Peltier operating parameters were continuously monitored. The experiment was conducted 15 times under identical conditions to ensure accuracy, with the cold surface and collection bucket cleaned and dried between experiments. All recorded data were analysed to determine steady-state values, and the average outcome of the 15 trials has been used to generate the values represented in the diagram. The water condensation increases with the increase of air velocity and relative humidity [23]. In the present work, the experimental work has been performed many times at an air velocity and relative humidity of 0.7 m/s and 70%, respectively, to get optimal results. The experimental results have been represented in Figure 8. The present study results in less surface area achieved with the one Peltier module than Kadhim 2020 [23] and Joshi 2017 [24].

A suitable surface and air properties are needed to condense the atmospheric air, which is flexible enough to slide the condensed droplets quickly from the surface and to nucleate new water droplets. A CS was designed in SALOME to perform the simulation. Therefore, a set of numerical simulations was performed using the finite volume method-based free and open-source computational fluid dynamics software OpenFOAM 2206 to calculate the water harvesting rate at various parameters. In previous studies, the water harvesting rate increased with the increase in relative humidity. However, WHR at different dry bulb temperatures may vary at different relative humidities and surface wettabilities. The condensing droplet nucleation and transportation vary with the CS wettability. This method was an alternative solution to analyze the water harvesting rate and droplet dynamics on the CS. The numerical approach has been explained in detail in the following section.

3. NUMERICAL APPROACH

3.1 Geometrical explanation of the problem

In the present study, a condensing CS in a hemispherical shape connected with two rectangular buckets at the end of the CS is used to collect water droplets. The water harvesting rate (WHR) has been calculated for two cases with respect to different relative humidities (RH's), Dry bulb temperatures (DBTs), and surface wettabilities. In the first case, WHR has been calculated for various DBTs when CS is maintained at constant surface wettability with variable RH's. Whereas, in the second case, the WHR has been calculated for various DBT's when CS is maintained at different surface wettabilities by keeping constant RH. Here, the surface wettability is defined by the contact angle between the water droplet and the surface. The range of the contact angle lies between $0° < \theta < 10°$, $10° < \theta < 90°$, $90° < \theta < 150°$, and $150° < \theta < 180°$, which are known as superhydrophilic, hydrophilic, hydrophobic, and superhydrophobic, respectively [25, 26].

Figure 3 shows the detailed information of a two-dimensional geometrical representation of a condensing CS with water collecting buckets that are used in the present study. The dimensions of the water collecting cup are considered as 0.005 m in height and 0.003 m in width, while the radius of the CS is taken as 0.015 m. The CS in hemispherical shape in the computational domain is exposed to the atmosphere to condense the humidity present in the atmospheric air into water droplets under various DBTs, RHs, and surface wettabilities. The condensed water droplets on the CS from the humid air slide/roll down to the connected buckets due to the

gravitational force [23].

Table 2 shows a brief description of the parameters considered in the present study to run the two cases. In the present simulation three DBT's (25 ℃, 30 ℃ and 35 ℃), five RH's (50%, 60%, 70%, 80% and 90%) and seven surface contact angles (0°, 30°, 60°, 90°, 120°, 150° and 180°) are considered to calculate WHR for both cases. Whereas the temperature of the CS has been maintained at 0 ℃ in both cases. In the first case, the WHR has been calculated for three DBT's at a constant surface contact angle of 0° by varying RH's from 50% to 90%. Whereas, in the second case, the WHR has been calculated for three DBT's at a constant relative humidity of 70% by varying surface contact angles from 0° to 180°. The value of partial vapor pressure (Pa) is obtained by giving DBT and RH as inputs in the psychrometric calculator [27]. The thermodynamic properties of saturated steam are known by giving partial vapor pressure as input in the piece software [28]. Similarly, at one bar pressure, the properties of saturated air are obtained by giving various dry bulb temperatures as input in the piece software [29].

3.2 Governing equations

In the present study, the volume of fluid (VOF) method is utilized to capture the interface of the surface. The governing equations of the VOF method are [30]:

Continuity equation:

$$\frac{\partial \rho}{\partial t} + \nabla . (\rho u) = 0 \tag{1}$$

Momentum equation:

$$\frac{\partial (\rho u)}{\partial t} + \nabla . (\rho u u) = -\nabla P + \nabla . \left[\mu_{eff} (\nabla u + (\nabla u)^T)\right] + \rho g + \vec{F}_\sigma \tag{2}$$

Energy equation:

$$\frac{\partial (\rho E)}{\partial t} + \nabla . [u(\rho E + P)] = \nabla . \left(k_{eff} \nabla T\right) + S \tag{3}$$

where, ρ, u, P, T, and g are the density, velocity, pressure, temperature, and acceleration due to gravity, respectively. The terms $\vec{F}_\sigma$, E, and S are the force of the surface tension, internal energy, and source term of phase transitions, respectively. The effective parameters μ_{eff} and k_{eff} are the effective dynamic viscosity and thermal conductivity, respectively. The effective parameters have been defined as follows:

$$\mu_{eff} = \mu_L + \mu_t \tag{4}$$

$$k_{eff} = k_L + k_t \tag{5}$$

In the above Eqs. (4) and (5), indices L and t represent laminar and turbulent flows, respectively.

The force of surface tension value is obtained by using the continuum surface force (CSF) model, which was proposed by Brackbill et al. [31].

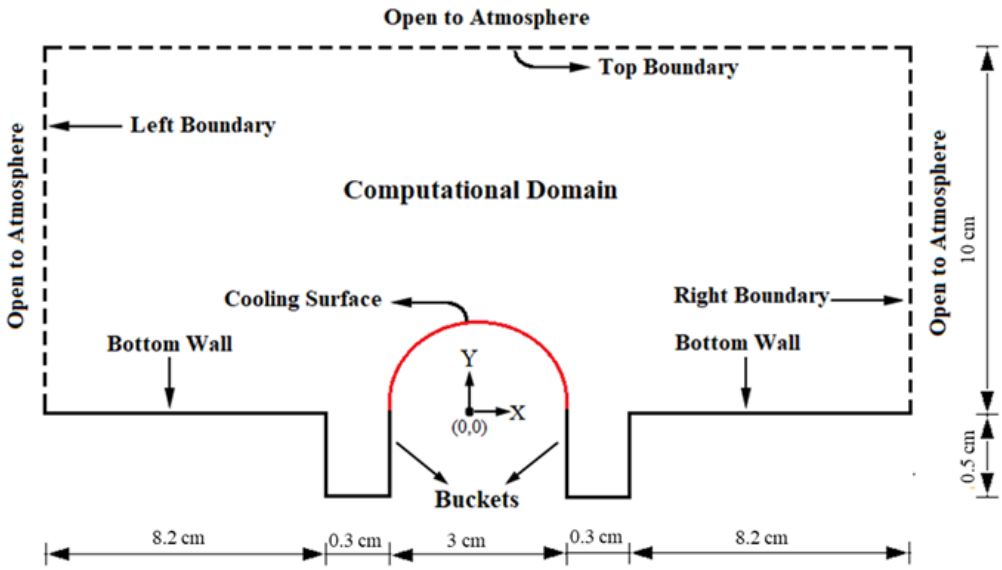

Figure 3. Schematic diagram of computational domain

Table 2. Parameter details of the simulation

S. No.	Parameters	Case 1	Case 2
1.	Curved surface (CS) temperature (T_s)	0 ℃	0 ℃
2.	Dry bulb temperature (DBT)	25 ℃, 30 ℃, 35 ℃	25 ℃, 30 ℃, 35 ℃
3.	Surface contact angle (θ)	0°	0°, 30°, 60°, 90°, 120°, 150° and 180°
4.	Relative humidity (RH %)	50%, 60%, 70%, 80% and 90%	70%
5.	Partial vapor pressure (PVP) and Saturated water properties	Based on DBT and RH	Based on DBT and RH
6.	Saturated air properties	At one bar pressure	At one bar pressure

$$F_\sigma = \sigma \frac{\alpha_l \rho_l k_v \nabla \alpha_v + \alpha_v \rho_v k_l \nabla \alpha_l}{\frac{1}{2}(\rho_v + \rho_l)} \quad (6)$$

where, σ represents the surface tension of water, k_l and k_v are defined as follows [31]:

$$k_l = \nabla \cdot \frac{\nabla \alpha_l}{|\nabla \alpha_l|} \quad (7)$$

$$k_v = \nabla \cdot \frac{\nabla \alpha_v}{|\nabla \alpha_v|} \quad (8)$$

In the above Eqs. (7) and (8), α is the volume fraction and subscripts l and v are the liquid and vapour phases, respectively. The sum of the volume fractions of liquid and vapour phases is unity in the computational grid; the equation is represented as:

$$\alpha_l + \alpha_v = 1 \quad (9)$$

The properties in the VOF method, which are viscosity, density, and thermal conductivity of the fluid, were defined as follows [30]:

$$\mu_m = \alpha_v \mu_v + (1 - \alpha_v)\mu_l \quad (10)$$

$$\rho_m = \alpha_v \rho_v + (1 - \alpha_v)\rho_l \quad (11)$$

$$k_m = \alpha_v k_v + (1 - \alpha_v)k_l \quad (12)$$

In the present study, shear stress transport (SST) $k - \omega$ Reynolds averaged Navier-stokes (RANS) approach is considered to analyse the two-dimensional, transient, incompressible flow fluid in the computational domain. The turbulent kinetic energy (k) and specific turbulent dissipation rate (ω) are estimated by using the governing equations of SST $k - \omega$ turbulence model, the equations are defined as follows [32]:

$$\frac{\partial(\rho k)}{\partial t} + \nabla \cdot (\rho u k) = \nabla \cdot \left[\left(\mu_L + \frac{\mu_t}{\sigma_k}\right)\nabla k\right] + G_k - Y_k \quad (13)$$

$$\frac{\partial(\rho \omega)}{\partial t} + \nabla \cdot (\rho u \omega) = \nabla \cdot \left[\left(\mu_L + \frac{\mu_t}{\sigma_\omega}\right)\nabla \omega\right] + G_\omega - Y_\omega \quad (14)$$

where, the terms G_k and Y_k are the generation and dissipation of turbulence kinetic energy due to mean velocity gradients, G_ω and Y_ω are the generation and dissipation of specific dissipation rate due to turbulence, respectively.

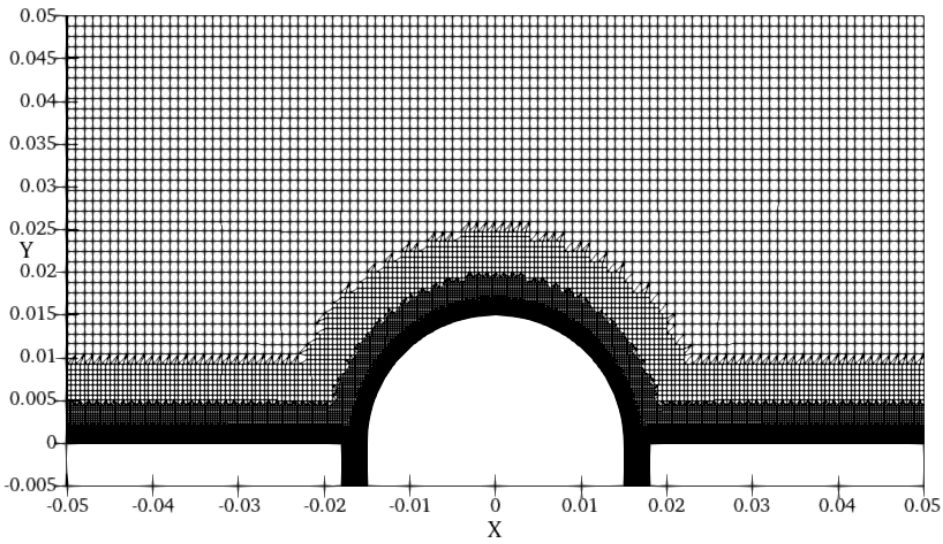

(a) Computational domain

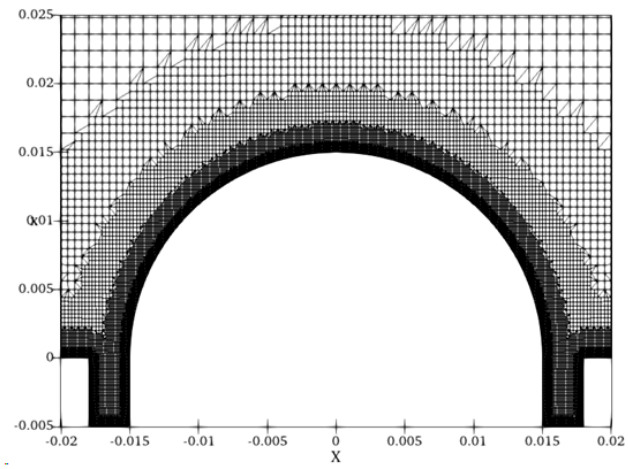

(b) Curved surface

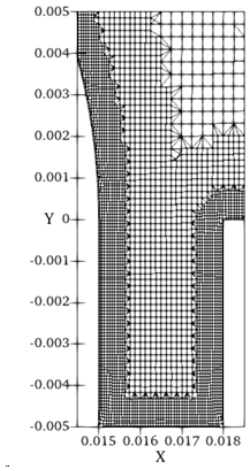

(c) Bucket

Figure 4. (a) Variation in grid distribution of computational domain, (b) Closed view of curved surface (CS), and (c) Closed view of bucket

3.3 Numerical schemes and boundary conditions

The governing equations are approximated by using the finite volume method in the present study. A first-order implicit scheme is utilized to discretize the transient terms in the governing equations. Whereas, convective and diffusion terms in the governing equations are approximated by the second-order upwind scheme and the second-order central differencing scheme, respectively. The coupling of pressure and velocity is achieved by choosing the PIMPLE algorithm with one inner and two outer corrector loops in each time step. Here, the PIMPLE algorithm is a combination of Pressure Implicit with Splitting of Operator (PISO) and Semi-Implicit Method for Pressure-Linked Equations (SIMPLE) algorithms. The pressure correction equation is discretized with a convergence criterion of 10^{-9} at each time step by using the geometric agglomerated algebraic multigrid (GAMG) solver. The remaining parameters are solved using a stabilized pre-conditioned bi-conjugate gradient (PBiCGStab) solver with a tolerance error of 10^{-7}. In the present transient simulation, the Courant number value is always maintained less than or equal to 0.5 at variable time steps to get an accurate solution. Courant number is calculated using the formula of $\left(\frac{|U|\Delta t}{\Delta x} \leq 0.5\right)$, where $|U|$ is the flow velocity, Δt is the time step and Δx is the mesh cell size. The numerical simulations are carried out using open-source CFD software, OpenFOAM (Open-source Field Operation and Manipulation).

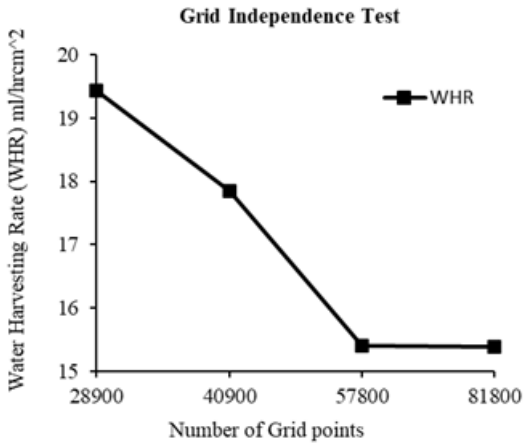

Figure 5. Variation of condensation rate for four different grid sizes

3.4 Grid independence tests

A mesh has been generated for the computational domain with a total of 8.18×10^4 grid points. With these grid points, a total of 1.57×10^5 faces and 3.8×10^4 cells have developed. Figure 4(a) shows the variation in grid distribution of the computational domain, which was formed with the total number of cells. Out of which 94.86% are of hexahedral type, 4.46% are of polyhedral type, and the rest 0.67% are of prism type. Computational iteration time reduces due to the major percentage of hexahedral cells. Polyhedral-type cells were seen at every transition state of the mesh, as shown in Figure 4(b). Maximum volume cells are located far from the boundary, and minimum volume boundaries are near the CS and walls, as shown in Figure 4(c). The volumes of the maximum and minimum cells of the computational domain are 4.81×10^{-9} and $2.23 \times 10^{-12,}$ respectively. The mesh maximum non-orthogonality is 37.54 to provide good computational results, with an average of 4.29. The maximum skewness of the mesh is limited to 2.12 with a maximum aspect ratio of 6.66.

Grid independence test has been conducted at DBT 30 ℃ and 70% RH at different grid sizes. Figure 5 represents the volume of water collected per second by varying the grid sizes of the computational domain. The volumes of WHR at 8.18×10^4 and 5.78×10^4 grid sizes are nearly similar, and we observed that a similar amount of WHR has been collected by further increasing the grid sizes in the computational domain. This indicates that the volume of WHR is independent of grid size after reaching the maximum number of grid points. A mesh with a maximum of 8.18×10^4 grid points has been considered for all the simulations in the present study to be on the safer side.

4. RESULTS AND DISCUSSIONS

A CS is used to analyse the mobility of condensed droplets on the surface, and the rate of water harvesting on the surface is determined by incorporating the parameters of DBT, surface wettability, and relative humidity. The condensing of water droplets on the CS depends on the humid air properties such as density, kinematic and dynamic viscosities, thermal conductivity, partial vapour pressure, dew point temperature, specific enthalpy, and specific heat. The shape and mobility of the droplets depend on the Prandtl number and surface tension of the surface. The present study considers a constant Prandtl number and surface tension (σ) of 0.7 and 0.07 N/m, respectively. At a particular DBT and RH, the values of partial vapor pressure and dew point temperature of atmospheric air are obtained from the psychrometric chart [27]. The remaining parameters for saturated water and air are obtained from the piece database [28, 29].

In the present study, two cases are considered to calculate the WHR on the CS, as shown in Table 3 and Table 4. All sets of simulations are carried out by varying the parameters such as DBT, RH, and surface wettabilities. The range of parameters is as follows: the dry bulb temperature (DBT) ranges from 25 ℃ to 35 ℃ with an interval of 5 ℃; the relative humidity ranges from 50% to 90% with an interval of 10%; and the surface contact angle ranges from 0° to 180° with an interval of 30°. In case 1, the three DBTs (25 ℃, 30 ℃, and 35 ℃) were subjected to five RHs (50%, 60%, 70%, 80%, and 90%) by keeping a constant water contact angle θ = 0°, as shown in Table 3. Whereas, in the case 2 set of simulations, three DBT's (25 ℃, 30 ℃, and 35 ℃) are subjected to seven different surface contact angles (0°, 30°, 60°, 90°, 120°,150°, and 180°) by keeping constant RH as 70%, as shown in Table 4.

These contact angles utilize a static approach over a dynamic one because of the slow condensation to calculate WHR. At the low velocities, the surface interface remains in a quasi-equilibrium state where the effects of dynamic wetting and contact angle hysteresis are negligible. Therefore, the static angle provides a reliable and computationally stable representation of the surface within the numerical model. Studying all these 36 sets of simulations with different parameters can provide a better understanding of the following topics:

- The behaviour of the condensed droplets, such as

sticking, rolling, and bouncing on the CS, which are influenced by the adhesive and cohesive forces, has been analysed.

- The water harvesting rate has been obtained for all sets of simulations, and a comparative study has been provided.

Table 3. List of all parameters considered in case 1 at constant WCA of $\theta = 0°$

S. No.	Dry Bulb Temperature (DBT °C)	Relative Humidity (RH %)
1	25	50, 60, 70, 80 and 90
2	30	50, 60, 70, 80 and 90
3	35	50, 60, 70, 80 and 90

Table 4. List of all parameters considered in case 2 at constant RH = 70%

S. No.	Dry Bulb Temperature (DBT °C)	Water Contact Angle (θ)
1	25	0°, 30°, 60°, 90°, 120°, 150° and 180°
2	30	0°, 30°, 60°, 90°, 120°, 150° and 180°
3	35	0°, 30°, 60°, 90°, 120°, 150°and 180°

4.1 Fundamental condensed droplet dynamics on the curved surface

Atmospheric water harvesting involves four main steps: 1. Condensation, 2. Coalescence, 3. Transportation and 4. Collection of water drops. Condensation of atmospheric air occurs due to factors such as dry bulb temperature, relative humidity, and surface temperature. The rest, coalescence, transportation, and collection of condensed water depend on the surface morphology, surface wettability, surface tension, viscosity, cohesive and adhesive forces, and acceleration due to gravity. In the present study, the condensed water droplet shape and mobility depend on the surface wettability. Surface wettability is categorised into four regions: superhydrophilic, hydrophilic, hydrophobic, and superhydrophobic regions. The range of the contact angle between the water droplet and the surface determines the wettability regions. The range of contact angles from 0° to 10°, 10° to 90°, 90° to 150°, and 150° to 180° is considered as the superhydrophilic, hydrophilic, hydrophobic, and superhydrophobic regions, respectively [23, 30, 31]. The condensed water characteristics on the CS for various parameters (DBT = 30 °C, RH = 70%, and $T_s = 0$ °C) at different surface wettabilities are illustrated in Figure 6.

In the present study, the CS has been simulated under various DBTs with different surface contact angles varying from 0° to 180° while keeping constant relative humidity. The condensation of water drops occurs on the CS due to the temperature difference between the atmospheric air and the CS. The shape and mobility of condensed water have been observed on the CS, which is subjected to four different wettability surfaces. Figure 6(a) shows the behaviour of the droplet (wetting characteristics) on the various wettability surfaces. The water dynamics on the surface are as follows: complete wetting on the superhydrophilic surface, incomplete wetting on the hydrophilic and hydrophobic surfaces, and non-wetting on the superhydrophobic surfaces [33, 34]. The outcome of the condensed water behaviour on the various wettability surfaces agrees with the theory explained by Lei and Guo [33]. Figure 6(c) shows the behaviour of the condensed water (red) on the CS at four different surface contact angles. These four $\theta = 0°$, 60°, 120°, and 150° surface contact angles are considered as the superhydrophilic, hydrophilic, hydrophobic, and superhydrophobic surfaces, respectively.

The superhydrophilic and hydrophilic surfaces have a strong ability to attract water from the atmosphere. The condensed water from the atmosphere adheres strongly to the superhydrophilic surface, and a continuous water film has been formed, as shown in Figure 6(b1). Whereas, a semi-circle water droplet shape has been observed on the hydrophilic surface, as shown in Figure 6(b2). The condensed water on these superhydrophilic and hydrophilic surfaces sticks strongly due to the strong adhesive forces rather than the cohesive forces between the water and the surface. The condensed water on the hydrophobic surface, a three-fourth of the circle shape, has appeared due to the less adhesive forces than the cohesive forces, as shown in Figure 6(b3). Whereas, a complete spherical shape has been observed on the superhydrophobic surface, as shown in Figure 6(b4).

The condensed water on the superhydrophilic surface sticks strongly and moves to the buckets along with the boundary of the CS, as shown in Figure 6(d1). The droplets on the hydrophilic surface coalesce with the adjacent droplets and then flow towards the buckets, as shown in Figure 6(d2). Whereas the condensed droplets roll down and jump over the hydrophobic and superhydrophobic surfaces, respectively. The droplets after reaching maximum volume on the hydrophobic surface roll down to the buckets due to the gravitational forces, as shown in Figure 6(d3). Whereas the condensed droplets roll and jump on the superhydrophobic surface, as shown in Figure 6(d4). Here, the adhesive forces cannot overcome the gravitational forces on the hydrophobic and superhydrophobic surfaces due to the smoothness of the surface. Hence, the droplets either roll or jump on the surfaces.

The qualitative condensed water droplet behaviours described in Section 4.1, specifically, the transition from film-wise condensation on superhydrophilic surfaces to fast gravity-driven condensation on hydrophobic and superhydrophobic surfaces. This provides a physical foundation for the water harvesting rate in the following section 4.2. The following section presents a quantitative analysis of WHR. The analysis is divided into two focused cases; the first case evaluates the WHR across varying RHs by keeping a constant superhydrophilic surface in Section 4.2.1. Subsequently, section 4.2.2 investigates the WHR across varying surface wettabilities by keeping constant RH.

4.2 Water harvesting rate (WHR) analysis for various DBT

Water harvesting rate has been calculated for all the cases considered in the present study, as shown in Table 2 and Table 3. The condensed water sticks, rolls, and bounces on the CS due to the action of adhesive and cohesive forces. After condensation, water slides down over the CS. The water has been collected into the buckets due to the action of the gravitational force, as shown in Figure 1. The height (h) of the collected condensed water in the buckets has been measured with time for all the cases. The volume of the condensed water in the buckets is calculated as $V = L * b * h$. Where L (Figure 1) and b represent the length and breadth of the collecting buckets, respectively. The height (h) represents the condensed

water height in the buckets. The length and breadth of the buckets are considered as 0.003 m and 0.01 m, respectively. The height of the bucket is calculated from the results of the simulation. The water harvesting rate is calculated in ml/sec by noting the height of collected water at a particular time using the formula:

$$Water\ harvesting\ rate\ (WHR) = \frac{Volume}{Time} \quad (15)$$

In the present study, the water harvesting rate has been calculated at different relative humidities and water contact angles for various DBT's.

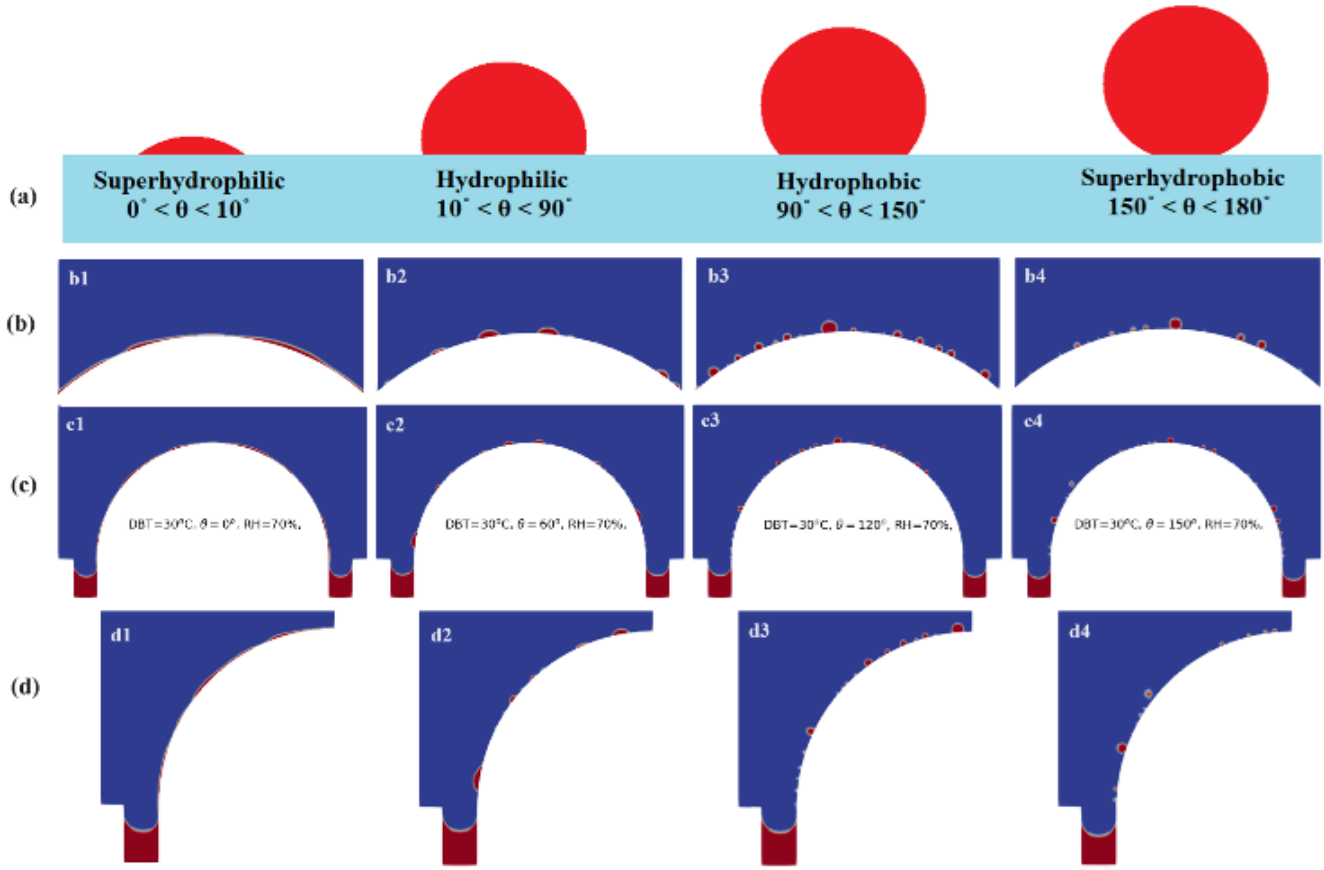

Figure 6. Shape and mobility of the condensed water on the curved surface (CS) w.r.t various surface wettabilities: (a) Shape of the condensed drop on the surface [27], (b) Zoomed view of the middle part of the curved surface (CS), (c) condensed water shape and mobility on the curved surface (CS) w.r.t various surface contact angles, and (d) zoomed view of the half portion of the curved surface (CS)

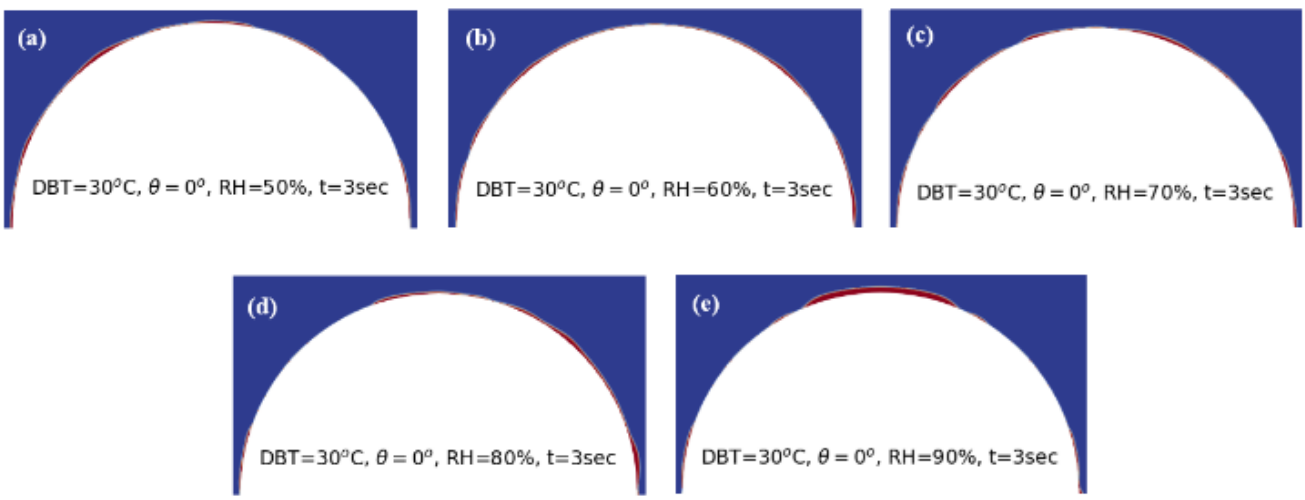

Figure 7. Condensed droplet behaviour on a superhydrophilic curved surface (CS) at 30 °C DBT with increasing relative humidity from 50% to 90%

4.2.1 Water harvesting rate analysis for various relative humidities

The condensation dynamics are quantitatively assessed based on the evolution of the structure of the surface, dry bulb temperature, surface wettability, and relative humidity. A detailed analysis of the condensation dynamics for a CS (θ = 0˚) provides a framework for various relative humidities and dry bulb temperatures. Figure 7 shows the condensed water droplets' behaviour on the superhydrophilic surface with corresponding relative humidities (50%, 60%, 70%, 80%, and 90%) at the DBT of 30 ℃. The surface having a contact angle theta = 0 exhibits a high surface energy, which helps to nucleate droplets more frequently. Due to the low contact angle, the condensed droplets coalesce and spread rapidly, forming a thin and continuous liquid film on the surface. The curved superhydrophilic surface enhances the drainage of condensed water droplets due to the acceleration of gravity.

When dealing with curved superhydrophilic surfaces, the influence of relative humidity on film-wise condensation is particularly significant. Figure 7(a) shows that the surface is at around 50% relative humidity, which experiences minimal condensation, often resulting in thin or nearly non-existent condensate films due to the limited vapor content in the air. As the humidity increases to the 60–70% range, condensation occurs more frequently, resulting in the formation of a homogenous thin layer that spreads stably along the CS, driven by significant surface wettability and capillary forces, as shown in Figure 7(b)–(c). The condensation rate is significantly increased at high relative humidity levels of 80-90%, resulting in the formation of thick, stable liquid films that may accumulate over time, as shown in Figure 7(d)–(e).

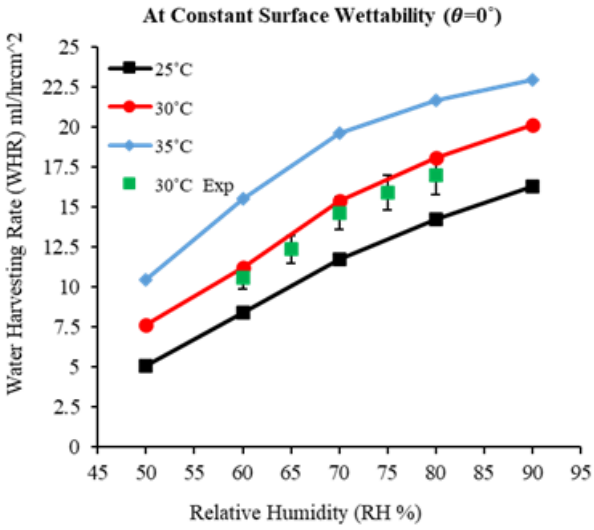

Figure 8. Effect of relative humidity on water harvesting rate at constant surface wettability

The condensation rate is strongly influenced by both relative humidity and dry bulb temperature, as these parameters are directly influenced by the vapor pressure difference between the curved superhydrophilic surface and the atmospheric air. The experimental results at 30 ℃ DBT, condensation rate increases from 10.615 ml/hrcm^2 at 60% RH to 16.958 ml/hrcm^2 at 80% RH. The simulation results at a 25 ℃ DBT, the condensation rate rises from 5.093 ml/hrcm^2 at 50% RH to 8.403 ml/hrcm^2 at 60%, 11.713 ml/hrcm^2 at 70%, 14.260 ml/hrcm^2 at 80%, and peaks around 16.297 ml/hrcm^2 at 90% RH. When the DBT increases to 30 ℃, the water harvesting rate grows correspondingly due to the high moisture-carrying capacity of warmer air, starting at 7.639 ml/hrcm^2 at 50% RH and rising to 20.117 ml/hrcm^2 at 90% RH. At an even higher DBT of 35 ℃, the water harvesting rate becomes more aggressive, starting at 10.440 ml/hrcm^2 for 50% RH and reaching the peak of 22.918 ml/hrcm^2 at 90% RH, as shown in Figure 8.

The experimental WHR measured at 30 ℃ DBT and 60-80% RH shows a rising trend, the results matching the trend predicted by the simulation results. The simulated values at 30 ℃ closely align with the experimental measurements, confirming that the model accurately captures the moisture-dependent behavior of the condensation process. These trends have been discovered using numerical simulation, which clearly shows how increased temperature enhances the effect of relative humidity on condensation. The simulation results offer valuable insights for the design and optimization of condensation-based systems in response to a variety of environmental conditions.

4.2.2 Water harvesting rate analysis at various water contact angles

In the present section, the condensation rate for three DBTs (25 ℃, 30 ℃, and 35 ℃) is analysed for various surface contact angles by keeping a constant relative humidity of 70%. The variation of the surface contact angle from 0° to 180° with an interval of 30° results in four surface wettability regions: superhydrophilic, hydrophilic, hydrophobic, and superhydrophobic regions. The variation of surface wettability affects the mobility of condensed droplets on the CS; the condensed droplets slide, roll, and bounce on the CS. The water harvesting rate for 25 ℃, 30 ℃, and 35 ℃ DBTs with variable surface wettabilities is represented in black, red, and blue colours, respectively, as shown in Figure 9.

At the DBT of 25℃, the superhydrophilic surface with CA = 0° has the highest water harvesting rate, with the value of 12.987 ml/hrcm^2. As the surface reaches the superhydrophobicity with a contact angle of 180°, the water harvesting rate progressively diminishes, ultimately reaching 7.894 ml/hrcm^2. A similar pattern was observed at the DBT of 30 ℃, where the harvesting rate began at 16.806 ml/hrcm^2 for a superhydrophilic surface and dropped to 14.158 ml/hrcm^2 at a contact angle of 180°. When the DBT is 35 ℃, the condensation is more aggressive because of the increased vapor pressure, and the highest harvesting rate is observed at the superhydrophilic surface of 0° contact angle with a value of ml/hrcm^2. As the surface reaches the superhydrophobicity of a contact angle of 180°, the harvesting rate decreased to 17.851 ml/hrcm^2. The overall pattern revealed that the surfaces with lower contact angles consistently displayed greater water harvesting capabilities. This effect was observed across all the dry bulb temperatures.

It is observed that the WHR reduces for superhydrophobic surfaces. This is attributed to the high nucleation density, causing moisture to form within the surface grooves. This promotes a transition from the Cassie-Baxter state to the Wenzel state, where the pinning force increases and prevents the droplet shedding by gravity, effectively flooding the surface. This leads to an increase in thermal resistance, thereby hindering further condensation. Whereas an ultra-thin film forms on the superhydrophilic surface. This reduces the thermal resistance and allows quick heat transfer between the vapour and the surface. The superhydrophilic surface uses the

Laplace pressure gradient to actively pull the condensed water towards the buckets. Consequently, the continuous capillary-driven condensing on the superhydrophilic surface outperforms the slow shedding on hydrophobic surface alternatives.

The percentage reduction in harvesting rate from 0° to 180° was roughly 39.2%, 15.76%, and 8.96% for the dry bulb temperatures of 25 °C, 30 °C, and 35 °C, respectively. This indicates that as ambient temperature increases, the influence of surface wettability on water harvesting rate decreases. At higher dry bulb temperatures, the harvesting rates are increased due to the higher vapor pressure, which partially mitigates the adverse impacts of greater contact angles. These simulation findings provide insights for optimizing surface design for atmospheric water harvesting systems.

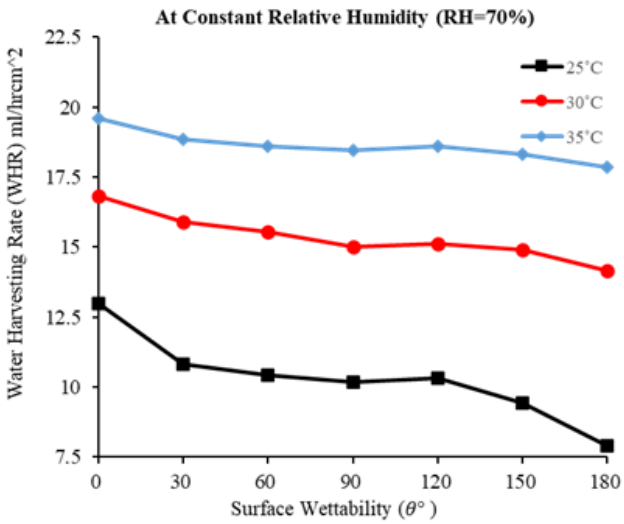

Figure 9. Effect of surface wettability on water harvesting rate at constant relative humidity

5. CONCLUSION

In the present study, experimental investigations were conducted on CS to evaluate the condensed droplet behaviour and water harvesting rate at various properties, such as dry bulb temperature and relative humidity. The present study mainly focused on the water harvesting rate and behaviour of the condensed water droplets with respect to dry bulb temperature, relative humidity, and surface wettability. The experimental findings clearly reveal that the CS achieves a higher water harvesting rate, 14.631 ml/hrcm^2. The high yield suggests that the CS geometry is an effective strategy to enhance WHR. The improved performance is achieved with greater droplet shedding and surface wettability, promoting continuous condensation and collection.

Complementing the experimental observations, a detailed two-dimensional numerical simulation was carried out using the Volume of Fluid method to analyse 36 different cases with different conditions of surface wettability, dry bulb temperature, and relative humidity. The numerical results strongly aligned with the experimental trends, confirming that the geometry of the surface, surface wettability, and ambient conditions considerably influence the water harvesting rate.

The condensation rate was found to increase substantially with both rising relative humidity and dry bulb temperature due to enhanced vapor pressure differentials. At 25 °C, the condensation rate increased from 5.093 ml/hrcm^2 at 50% RH to 16.297 ml/hrcm^2 at 90% RH, while at 35 °C, it rose from 10.440 ml/hrcm^2 to 22.918 ml/hrcm^2 under the same RH range. This trend confirms that higher DBTs enhance moisture availability, thereby improving harvesting rates. The numerical analysis of condensation across varying surface wettabilities and DBTs (25 °C, 30 °C, and 35 °C) under a constant RH of 70% reveals that water harvesting performance is strongly influenced by surface contact angle. Superhydrophilic surfaces (θ = 0°) consistently yielded the highest condensation rates across all DBT's, with maximum values of 12.987 ml/hrcm^2, 16.806 ml/hrcm^2, and 19.608 ml/hrcm^2 at 25 °C, 30 °C, and 35 °C, respectively. In contrast, superhydrophobic surfaces (θ = 180°) showed reduced harvesting rates.

Overall, the integrated experimental and numerical findings provide a comprehensive understanding of the mobility of condensed water droplets and condensation performance on CSs. These insights can be instrumental in optimizing the design of efficient water harvesting systems and enhancing condensation-driven thermal management technologies.

REFERENCES

[1] Zhuang, S., Qi, H., Wang, X., Li, X., Liu, K., Liu, J., Zhang, H. (2021). Advances in solar-driven hygroscopic water harvesting. Global Challenges, 5(1): 2000085. https://doi.org/10.1002/gch2.202000085

[2] Raveesh, G., Goyal, R., Tyagi, S.K. (2021). Advances in atmospheric water generation technologies. Energy Conversion and Management, 239: 114226. https://doi.org/10.1016/j.enconman.2021.114226

[3] Christoforidou, M., Borghuis, G., Seijger, C., Van Halsema, G.E., Hellegers, P. (2023). Food security under water scarcity: A comparative analysis of Egypt and Jordan: Food security under water scarcity: Cases of Egypt and Jordan. Food Security, 15(1): 171-185. https://doi.org/10.1007/s12571-022-01310-y

[4] O. Access, Book_Sultan_2021_Book_Chapter_Adsorption-Based_Atmospheric_Water_Harvesting_Tech.pdf.

[5] Parker, A.R., Lawrence, C.R. (2001). Some beetles in the Namib Desert collect drinking water from fog-laden wind on their backs. Nature, 414: 33-34.

[6] Nørgaard, T., Dacke, M. (2010). Fog-basking behaviour and water collection efficiency in Namib Desert Darkling beetles. Frontiers in Zoology, 7(1): 23. https://doi.org/10.1186/1742-9994-7-23

[7] Zheng, Y., Bai, H., Huang, Z., Tian, X., Nie, F.Q., Zhao, Y., Zhai, J., Jiang, L. (2010). Directional water collection on wetted spider silk. Nature, 463(7281): 640-643. https://doi.org/10.1038/nature08729

[8] Ju, J., Bai, H., Zheng, Y., Zhao, T., Fang, R., Jiang, L. (2012). A multi-structural and multi-functional integrated fog collection system in cactus. Nature Communications, 3(1): 1247. https://doi.org/10.1038/ncomms2253

[9] Xie, J., Xu, J., Li, X., Liu, H. (2019). Dropwise condensation on superhydrophobic nanostructure surface, Part I: Long-term operation and nanostructure failure. International Journal of Heat and Mass Transfer, 129: 86-95.

https://doi.org/10.1016/j.ijheatmasstransfer.2018.09.100
[10] Khojasteh, D., Kazerooni, M., Salarian, S., Kamali, R. (2016). Droplet impact on superhydrophobic surfaces: A review of recent developments. Journal of Industrial and Engineering Chemistry, 42: 1-14. https://doi.org/10.1016/j.jiec.2016.07.027
[11] Yoshimitsu, Z., Nakajima, A., Watanabe, T., Hashimoto, K. (2002). Effects of surface structure on the hydrophobicity and sliding behavior of water droplets. Langmuir, 18(15): 5818-5822. https://doi.org/10.1021/la020088p
[12] Peng, B., Ma, X., Lan, Z., Xu, W., Wen, R. (2015). Experimental investigation on steam condensation heat transfer enhancement with vertically patterned hydrophobic–hydrophilic hybrid surfaces. International Journal of Heat and Mass Transfer, 83: 27-38. https://doi.org/10.1016/j.ijheatmasstransfer.2014.11.069
[13] Hasan, A.H., Banooni, S.M., Habeeb, L.J. (2023). Enhanced performance of structurally optimized plate-fin heat exchangers through numerical modeling of heat transfer and pressure drop. Journal of Sustainability for Energy, 2(2): 39-50. https://doi.org/10.56578/jse020201
[14] Fadhl, H.H., Habeeb, L.J. (2024). Enhancement of pool boiling heat transfer via water-based nanofluids and multi-finned surface geometries. Journal of Sustainability for Energy, 3(2): 105-118. https://doi.org/10.56578/jse030204
[15] Rioboo, R., Voué, M., Vaillant, A., De Coninck, J. (2008). Drop impact on porous superhydrophobic polymer surfaces. Langmuir, 24(24): 14074-14077. https://doi.org/10.1021/la802897g
[16] Rykaczewski, K. (2012). Microdroplet growth mechanism during water condensation on superhydrophobic surfaces. Langmuir, 28(20): 7720-7729. https://doi.org/10.1021/la301618h
[17] Yanagisawa, K., Sakai, M., Isobe, T. (2014). Investigation of droplet jumping on superhydrophobic coatings during dew condensation by the observation from two directions. Applied Surface Science, 315: 212-221. https://doi.org/10.1016/j.apsusc.2014.07.120
[18] Weisensee, P.B., Tian, J., Miljkovic, N., King, W.P. (2016). Water droplet impact on elastic superhydrophobic surfaces. Scientific Reports, 6(1): 30328. https://doi.org/10.1038/srep30328
[19] Mondal, B., Jiao, K., Li, X. (2011). Three-dimensional simulation of water droplet movement in PEM fuel cell flow channels with hydrophilic surfaces. International Journal of Energy Research, 35(13): 1200-1212. https://doi.org/10.1002/er.1776
[20] Oestreich, J.L., Van Der Geld, C.W.M., Oliveira, J.G., Da Silva, A.K. (2019). Experimental condensation study of vertical superhydrophobic surfaces assisted by hydrophilic constructal-like patterns. International Journal of Thermal Sciences, 135: 319-330. https://doi.org/10.1016/j.ijthermalsci.2018.09.024
[21] Baghel, V., Sikarwar, B.S., Muralidhar, K. (2020). Dropwise condensation from moist air over a hydrophobic metallic substrate. Applied Thermal Engineering, 181: 115733. https://doi.org/10.1016/j.applthermaleng.2020.115733
[22] Seo, D., Lee, J., Lee, C., Nam, Y. (2016). The effects of surface wettability on the fog and dew moisture harvesting performance on tubular surfaces. Scientific Reports, 6(1): 24276. https://doi.org/10.1038/srep24276
[23] Kadhim, T.J., Abbas, A.K., Kadhim, H.J. (2020). Experimental study of atmospheric water collection powered by solar energy using the Peltier effect. IOP Conference Series: Materials Science and Engineering, 671(1): 012155. https://doi.org/10.1088/1757-899X/671/1/012155
[24] Joshi, V.P., Joshi, V.S., Kothari, H.A., Mahajan, M.D., Chaudhari, M.B., Sant, K.D. (2017). Experimental investigations on a portable fresh water generator using a thermoelectric cooler. Energy Procedia, 109: 161-166. https://doi.org/10.1016/j.egypro.2017.03.085
[25] Law, K.Y. (2014). Definitions for hydrophilicity, hydrophobicity, and superhydrophobicity: Getting the basics right. The Journal of Physical Chemistry Letters, 5(4): 686-688. https://doi.org/10.1021/jz402762h
[26] Drelich, J., Chibowski, E. (2010). Superhydrophilic and superwetting surfaces: Definition and mechanisms of control. Langmuir, 26(24): 18621-18623. https://doi.org/10.1021/la1039893
[27] Psychrometric calculator. https://www.kwangu.com/work/psychrometric.htm.
[28] Saturated water properties. https://www.peacesoftware.de/einigewerte/wasser_dampf_e.html.
[29] Saturated air properties. https://www.peacesoftware.de/einigewerte/luft_e.html.
[30] Hirt, C.W., Nichols, B.D. (1981). Volume of fluid (VOF) method for the dynamics of free boundaries ☆. Journal of Computational Physics, 39(1): 201-225. https://doi.org/10.1016/0021-9991(81)90145-5
[31] Brackbill, J.U., Kothe, D.B., Zemach, C. (1992). A continuum method for modeling surface tension. Journal of Computational Physics, 100(2): 335-354. https://doi.org/10.1016/0021-9991(92)90240-Y
[32] Menter, F.R. (1994). Two-equation eddy-viscosity turbulence models for engineering applications. AIAA Journal, 32(8): 1598-1605. https://doi.org/10.2514/3.12149
[33] Lei, J., Guo, Z. (2020). A fog-collecting surface mimicking the Namib beetle: Its water collection efficiency and influencing factors. Nanoscale, 12(13): 6921-6936. https://doi.org/10.1039/c9nr10808d
[34] Liu, J., Liu, S. (2019). Dynamics behaviors of droplet on hydrophobic surfaces driven by electric field. Micromachines, 10(11): 778. https://doi.org/10.3390/mi10110778

NOMENCLATURE

WHR	water harvesting rate
RH	relative humidity
CS	curved surface
VOF	volume of fluid
DBT	dry bulb temperature
θ	surface wettability
A	ampere
V	voltage
ρ	density
u	velocity
t	time
T	temperature
P	pressure
g	acceleration due to gravity

F_σ	force of the surface tension	**Subscripts**	
E	internal energy		
S	source term of phase transitions	L	laminar
μ_{eff}	effective dynamic velocity	t	turbulent
k_{eff}	effective thermal conductivity	l	liquid
σ	surface tension	v	vapour
α	volume of fraction		